

Optimization designs of artificial facilities in deserts based on computational simulation

DUN Hongchao, HUANG Ning*, ZHANG Jie*

Key Laboratory of Mechanics on Disaster and Environment in Western China, Lanzhou University, Lanzhou 730000, China

Abstract: Sediment transport of sand particles by wind is one of the main processes leading to desertification in arid regions, which severely impairs the ability of mankind to produce and live by drifting sand into settlements. Optimization designs of artificial facilities have lately attracted extensive interest for human settlement systems in deserts because of their acceptable protection effect, convenience of implementation, and low material cost. However, the complexity of a settlement system poses challenges concerning finding suitable materials, artificial facilities, and optimization designs for sand deposition protection. In an effort to overcome these challenges, we propose a settlement system built with brick, solar panel, and building arrays to meet the basic needs of human settlements in arid regions while preventing wind-sand disasters. The wind flow and movement characteristics of sand particles in the brick, panel, and building arrays were calculated using computational fluid dynamics and discrete phase model. The performance of three types of arrays in wind-sand flow in terms of decreasing the wind velocity and sand-particle invasion distance was evaluated. The results show that the wind velocity near the surface and the sand invasion distance were significantly decreased in the space between the brick arrays through properly selected vertical size and interspaces, indicating that the brick arrays have an impressive sand fixing and blocking performance; their effective protection distance was 3–4 m. The building arrays increased the near-surface wind velocity among buildings, resulting in less deposition of sand particles. The solar panel arrays were similar to the building arrays in most cases, but the deposition of sand particles on solar panels exerted a negative effect on energy utilization efficiency. Therefore, taking the optimal configuration of the settlement system into consideration, this study concludes that (1) brick arrays, which were proven effective in preventing sand particles, must be arranged in an upwind area; (2) solar panel arrays could accelerate the wind flow, so they are best to be arranged at the place where sand particles deposited easily; and (3) building arrays present a better arrangement in downwind areas.

Keywords: desert city; sand deposition; optimization; wind flow; sand movement

1 Introduction

Desertification is one of the most serious environmental problems around the world, intensifying sediment transportation by wind and leading to desert extension (Christopherson et al., 2009; Tsuchiya et al., 2010). The desert area accounts for 20% of the Earth's land area and is continuously expanding rapidly. Approximately 0.75×10^9 people are currently living in arid regions worldwide, and the growing population density adds pressure to the ecological environment (Warner, 2004).

*Corresponding authors: HUANG Ning (huangn@lzu.edu.cn); ZHANG Jie (zhang-j@lzu.edu.cn)

Received 2020-10-29; revised 2021-01-07; accepted 2021-01-18

© Xinjiang Institute of Ecology and Geography, Chinese Academy of Sciences, Science Press and Springer-Verlag GmbH Germany, part of Springer Nature 2021

Specifically, in Xinjiang Uygur Autonomous Region of China, the construction of a new countryside was carried out in the past few years to improve the quality of human life. Therefore, it is desirable to investigate wind flow and sediment transportation in human settlements (Golany, 1978).

The number of theoretical and experimental studies on novel tiled barriers for sand encroachment protection has notably increased, e.g., low-height sand fences (Hatanaka and Hotta, 1997; Bitog et al., 2009; Pye and Tsoar, 2009; Wang et al., 2017), straw checkerboard barriers (Wang and Zheng, 2002; Huang et al., 2013; Bo et al., 2015; Xu et al., 2018; Wang et al., 2020), clay barriers (Sun et al., 2012), plastic checkerboard barriers (Liu et al., 2011; Tian et al., 2015), and brick arrays (Zhao et al., 2012). A tiled barrier is usually low in height because 90% of sand grains encountering aerodynamic entrainment are located within 10–50 cm above the ground (Raupach and Lu, 2004; Mohamed and Khalaf, 2005; Jiang et al., 2017; Dun et al., 2018). The straw checkerboard barrier is a typical tiled barrier that is widely used to prevent sand disasters along the railway in China. The study of sand transport and deposit processes in straw checkerboard barriers has been promoted by simplified theoretical analysis (Wang and Zheng, 2002) and air-particle two-phase flow simulation (Huang et al., 2013; Xu et al., 2018). As the latest development, Xu et al. (2018) simulated the wind-sand flow around straw checkerboard barriers using a large eddy simulation and the particle-trajectory method to explore the turbulent flow characteristics, sand particle transport, and deposit processes. They found that there are huge single streamwise vortices that filled the internal space of straw checkerboard barrier cells and double spanwise vortices located in the back of the cells.

Considering the important role of the porous parameter in the sand fence effect (Lee and Lim, 2001), Zhang et al. (2010) studied the shelter effect of a porous fence on wind-sand flow using a high-speed digital camera and the particle-tracking velocimetry method. These studies found that the transport rate and kinetic energy of sand can be reduced by more than 80% and 90%, respectively. Inspired by this, Chen et al. (2012) experimentally and numerically studied the shelter effect of porous sand fences, and found that deflector-porous fence with 30% porosity, 150 mm height and 150 mm distance which between the fence and the prism model was most effective in controlling dust emission. Adopting the advantages of the two aforementioned main tiled barriers, a brick array made of clay has attracted considerable interest because of its acceptable effect, easy implementation, environmental friendliness, and low cost (Zhao et al., 2012). However, despite these advantages, the development of brick arrays is mainly retarded by a lack of thorough analysis of the sand particle transport and deposit processes.

Artificial facilities, such as buildings and solar panels, have significant influences on the atmospheric boundary-layer flow, but most simulations of the flow field around obstacles only model the flow field around isolated structures rather than groups of obstacles (Lien et al., 2004). For example, many scholars, based on the Reynolds-averaged Navier-Stokes (RANS) method, calculated the flow field around an isolated building (Montazeri and Blocken, 2013; Blocken, 2014; Chiu et al., 2017) and around two interactive buildings (Ramponi and Blocken, 2012; Behrouzi et al., 2014). Hunter et al. (1990) calculated the three-dimension (3-D) characteristics of the flow field within an urban canyon based on the turbulence model. In addition, the shortage of studies on sand-particle movement characteristics among groups of buildings limits the optimization design effect.

In this study, we propose a human settlement system referring to a previous study on a desert city (Golany, 1978). The system includes brick, solar panel, and building arrays to meet the basic needs for wind-sand disaster prevention, electric power, and human settlements. All these elements can also work together to prevent sand encroachment. To obtain the best arrangement of these facilities, we calculated the 3-D turbulent wind flow and sand-particle movement characteristics around the brick, solar panel, and building arrays using the computational fluid dynamics (CFD)-discrete phase model (DPM) method. The effects of the three kinds of arrays in wind-sand flow to decrease the mean air velocity and sand particle invasion distance were evaluated.

2 Model description

2.1 Fluid-phase governing equations

2.1.1 3-D Reynolds-averaged Navier-Stokes (RANS) equations

The present study assumes that the fluid flow satisfies the continuity equation and 3-D RANS momentum equation and that a neutral atmospheric boundary layer exists in the flow field. Heat and mass transfer processes are not considered. In addition, the model is simplified by assuming a non-slip boundary condition at the ground and an incompressible fluid flow with a constant density of $\rho=1.225 \text{ kg/m}^3$ and viscosity of $\mu=0.01789 \text{ g/(m}\cdot\text{s)}$.

The continuity equation is expressed as:

$$\frac{\partial u_i}{\partial x_i} = 0, \quad (1)$$

where u_i and x_i denote the fluid velocity (m/s) and the microelement position from the origin (m) in the i^{th} direction, respectively.

The momentum equation is listed as follows (Batchelor, 1967):

$$A = -\rho \overline{u_i u_j}, \quad (2)$$

$$\frac{\partial(\rho u_i u_j)}{\partial x_j} = -\frac{\partial p}{\partial x_i} + \mu \frac{\partial^2 u_i}{\partial^2 x_j} + \frac{\partial(-A)}{\partial x_j} + F_s, \quad (3)$$

$$F_s = -\sum_{i=1}^n F_{Di} / V_{\text{cell}}, \quad (4)$$

where A is the Reynolds stress caused by turbulence (Pa); p is the static pressure (Pa); F_s is the reactive force from sand particles (N); V_{cell} is the volume of a fluid grid cell (m^3); n is the number of sand particles in the grid cell; and F_{Di} is the drag force acting on a single sand particle by air flow (N).

2.1.2 Turbulence model

The turbulence flow was simulated using the renormalization group (RNG) k - ε turbulence model, which is good at predicting the behavior of complex flows. The complete formulation of the RNG k - ε turbulence model is given as follows (Yakhot and Orszag, 1986):

$$\frac{\partial(\rho k)}{\partial t} + u_i \frac{\partial(\rho k)}{\partial x_i} = \frac{\partial}{\partial x_i} \left(\frac{\mu_t}{\sigma_k} \frac{\partial k}{\partial x_i} \right) + G_k - \rho \varepsilon, \quad (5)$$

$$\frac{\partial(\rho \varepsilon)}{\partial t} + u_i \frac{\partial(\rho \varepsilon)}{\partial x_i} = \frac{\partial}{\partial x_i} \left(\frac{\mu_t}{\sigma_\varepsilon} \frac{\partial \varepsilon}{\partial x_i} \right) + \frac{C_{1\varepsilon}}{k} G_k - C_{2\varepsilon}^* \rho \frac{\varepsilon^2}{k}, \quad (6)$$

$$G_k = 2\mu_t S_{ij} S_{ij}, \quad (7)$$

$$C_{2\varepsilon}^* = C_{2\varepsilon} + C_{2\varepsilon}', \quad (8)$$

$$C_{2\varepsilon}' = C_\mu \rho \eta^3 (1 - \eta / \eta_0) / (1 + \beta \eta^3), \quad (9)$$

$$\mu_t = C_\mu \rho k^2 / \varepsilon, \quad (10)$$

$$\eta = \sqrt{2E_{ij} \times E_{ij}} k / \varepsilon, \quad (11)$$

$$E_{ij} = (\partial u_i / \partial x_j + \partial u_j / \partial x_i) / 2, \quad (12)$$

where k is the kinetic energy (m^2/s^2); ε is the kinetic-energy dissipation rate (m^2/s^3); σ_k and σ_ε are the Prandtl number of the kinetic energy and dissipation rate, respectively; S_{ij} is the shearing-rate tensor (Pa); G_k presents the generation of turbulence kinetic energy due to mean velocity gradients ($\text{kg}/(\text{m}\cdot\text{s}^3)$); $C_{2\varepsilon}^*$ and $C_{2\varepsilon}'$ are coefficients related to air density; E_{ij} is the mean strain rate; η is the coefficient of E_{ij} ; and μ_t is the turbulence viscosity. The default values of the coefficients used in the transport equation for k and ε are as follows: $C_\mu=0.085$; $C_{1\varepsilon}=1.42$; $C_{2\varepsilon}=1.68$; $\sigma_k=0.72$; $\sigma_\varepsilon=1.0$;

$\beta=0.012$; $\eta_0=4.38$.

2.2 Sand-particle kinetic equation

It is assumed that the forces applied to a single sand particle are gravity (F_g) and the drag force (F_D) of the fluid, and the two forces are expressed as follows (Huang et al., 2019):

$$F_g = \pi \rho_p D^3 g / 6, \quad (13)$$

$$F_D = C_D \pi D^2 \rho |V_r| V_r / 8, \quad (14)$$

$$C_D = (0.63 + 4.8 / Re^{0.5})^2, \quad (15)$$

$$Re = V_f \rho D |V_r| V_r, \quad (16)$$

$$V_r = \sqrt{(u - u_D)^2 + (v - v_D)^2 + (w - w_D)^2}, \quad (17)$$

where ρ_p is the particle density (kg/m^3); D is the particle diameter (m); g is the gravitational acceleration (9.8 m/s^2); C_D is the fluid drag coefficient; Re is the Reynolds number; and V_r is the relative velocity (m/s). In addition, u , v , and w are the three velocity components of air in the x , y , and z directions, respectively. u_D , v_D , and w_D are the three velocity components (m/s) of the sand particle in the x , y , and z directions, respectively.

The kinetic equation for sand particles is (Huang et al., 2013):

$$m_p \frac{dU_D}{dt} = F_g + F_D, \quad (18)$$

where m_p and U_D are the mass (kg) and velocity (m/s) of sand particle, respectively.

2.3 Numerical simulation method

The simulations were performed using the commercially available software package FLUENT (ANSYS company, USA). In the solution procedure, the nonlinear partial differential equations of the model were discretized using the finite volume method, and the segregated solution algorithm was selected. The pressure and velocity fields were decoupled using the semi-implicit method for pressure-linked equations (SIMPLE) method. The discrete phase model was used to solve the sand-particle movements. The fluid-phase governing equations and the kinetic equation of the sand particles were also decoupled in this study.

2.4 Computational domain and boundary conditions

A system includes brick, solar panel, and building arrays to meet the basic needs for wind-sand disaster prevention, electric power, and human settlements has been proposed in this work (Fig. 1). Brick arrays are located outside the desert city to prevent the wind-sand disaster; solar panel arrays, commercial district, industrial district and lake are set on the edge of the desert city to provide limited protection; building arrays are the core of the desert city to meet the basic needs of human settlements. All the arrays are single layer in vertical direction.

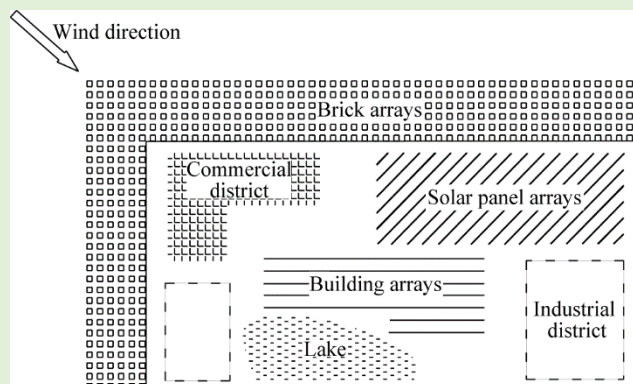


Fig. 1 A schematic diagram of a settlement system including brick, solar panel, and building arrays

Figure 2 presents the schematic illustration of the computational domains of the 3-D model in the simulation based on the assumption that the velocity of the wind field at the inlet meets the following logarithmic velocity profile:

$$U(z) = \frac{u_*}{k} \ln \frac{z}{z_0}, \quad (19)$$

where z is the height of fluid microelement (m); z_0 is the flat surface roughness (m); k is the von Karman constant (0.41); and u_* is the friction velocity (m/s).

The pressure at the outlet was specified as the reference. The symmetry boundary condition was used for the lateral computational domain, and a non-slip wall boundary condition was used for the ground and surfaces of the brick, solar panel, and building arrays (Fig. 2). The convergence criterion for the RNG $k-\varepsilon$ turbulence model was having residuals less than 1×10^{-6} .

In the simulations, the sand particles were placed 1 m before these arrays as a line at a density of 5×10^4 per meter. The sand-particle diameter was 0.2 mm. All the sand particles had an upward velocity in the range of 0.067–1.500 m/s as the initial condition, and obeyed a probability density function depending on the velocity as follows (Huang et al., 2006):

$$p(w_D) = \frac{1}{-0.624 + 1.81u_*} \exp\left(\frac{w_D}{-0.624 + 1.81u_*}\right). \quad (20)$$

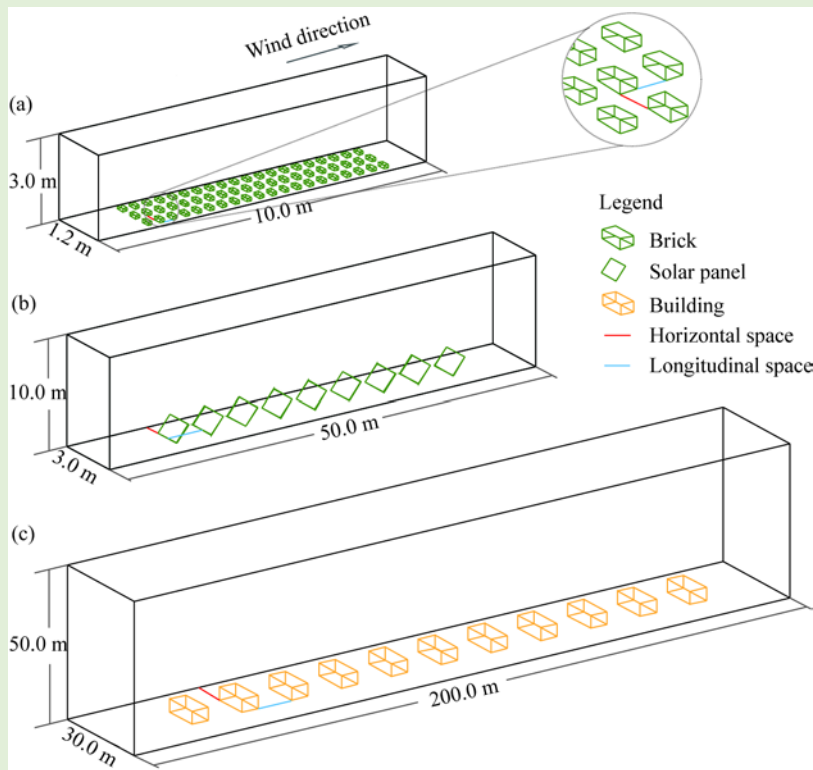


Fig. 2 Schematic sketch of brick arrays (a), solar panel arrays (b), and building arrays (c) on the computational domain and boundary conditions. Sand particles are blown into the simulation models from the left as the wind direction.

2.5 Grid system

To achieve a satisfactory trade-off between the computational cost and the need for capturing significant variations in the flow field, we used a hybrid grid system to mesh the computational domain. The domain was split into two zones: the upper zone was meshed with hexahedron grids, and the lower zone was meshed with tetrahedron grids.

Further, we applied the inflation method to the boundary cells to reflect the physical phenomena

at the boundaries correctly. The computational grids maintained a warping factor below 0.25, and the maximum aspect radius of the grids was less than 40. As a whole, the grids comprised approximately 2.0×10^6 individual cells.

2.6 Numerical validation

The numerical method was tested in four cases in which the wind flowed over a rough block surface. The height, breadth, and separation distance of the block are denoted as h , l , and d , respectively (m). The roughness concentration λ , which is defined as the ratio of frontal area to floor area per block, was calculated as Equation 21.

$$\lambda = hl / d^2. \quad (21)$$

The roughness length z_h was computed from the wind profile. Figure 3 shows that the calculated curve of roughness length z_h normalized with height h versus roughness concentration λ is in good agreement with the experimental curve reported by Raupach et al. (1980).

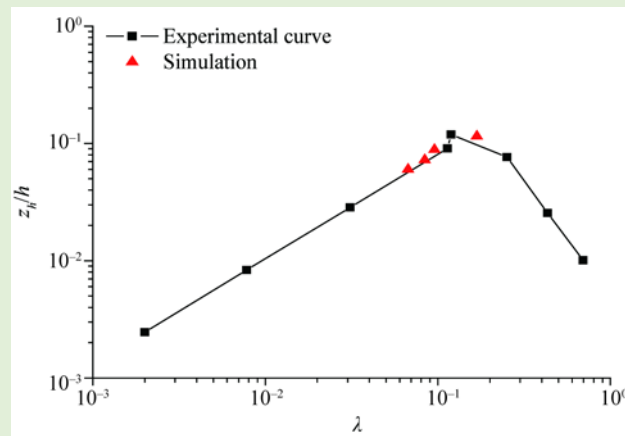


Fig. 3 Roughness length z_h normalized with height (h) versus roughness concentration (λ)

3 Results and discussion

In the simulations, the longitudinal direction was the same as the streamwise direction, and the horizontal direction was the transverse direction. To evaluate the performance of each type of array on fixing and blocking sand particles, we defined the average of velocities in the plane 0.02 m above the ground as mean velocity of sand particles (Dun et al., 2018), and the longest movement distance of sand particles in the arrays as invasion distance. All the simulated cases are listed in Table 1, and the parameters were sizes of elements, separation distance among the brick, solar panel, building arrays, and panel laying angle. In this section, the influence of frictional velocity on the wind flow and invasion distance of sand particles were also discussed.

3.1 Brick arrays

Figure 4 shows the flow velocity field and movement of sand particles in the brick arrays. As shown in Figure 4a, a series of eddies emerged within the brick arrays, and the velocity of air flow was significantly reduced comparing with the air above the bricks. In comparison, straw checkerboard barriers consisted of continuous lattice structures that forced the air flow over the slides and resulted in a series of progressively smaller eddies in the streamwise direction (Huang et al., 2013; Xu et al., 2018), while the air flow can bypass bricks owing to the space between individual bricks. Therefore, the sizes of eddies were smaller and the wind flow near the surface at different positions was more uniform than that over straw checkerboard barriers. Figure 4b presents the movement characteristics of the sand particles around the brick arrays. These sand particles moved forward in the interspaces between the bricks, and the number of sand particles in air clearly decreased, indicating that more sand particles were deposited on the surface. This movement form

Table 1 Changes in the spaces, sizes, angles, and friction velocity of the three types of arrays

Type of arrays	Horizontal space (m)	Longitudinal space (m)	Horizontal size (m)	Longitudinal size (m)	Vertical size (m)	Angle (°)	u_* (m/s)
Brick arrays	0.20	0.30	0.10	0.05	0.10	90	0.3
	0.30	0.40	0.15	0.10	0.15	90	0.4
	0.40	0.50	0.20	0.15	0.20	90	0.5
	0.50	0.60	0.25	0.20	0.25	90	0.6
	0.60	0.70	0.30	0.25	0.30	90	0.7
Solar panel arrays	0.00	0.10	-	0.05	0.10	15	0.3
	0.05	0.15	-	0.10	0.15	30	0.4
	0.10	0.20	-	0.15	0.20	45	0.5
	0.15	0.25	-	0.20	0.25	60	0.6
	-	0.30	-	0.25	0.30	75	0.7
Building arrays	10.00	10.00	10.00	10.00	3.00	90	0.3
	20.00	20.00	20.00	20.00	10.00	90	0.4
	30.00	30.00	30.00	30.00	17.00	90	0.5
	40.00	40.00	40.00	40.00	24.00	90	0.6
	50.00	50.00	50.00	50.00	30.00	90	0.7

Note: Horizontal space, separation distance between elements on horizontal direction; longitudinal space, separation distance between elements on longitudinal direction; angle, solar panel laying angle; u_* , friction velocity; -, no data.

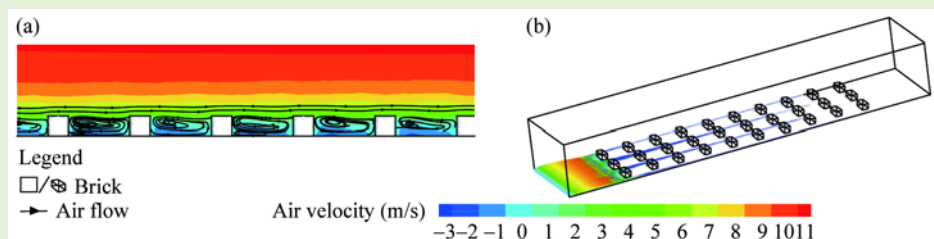


Fig. 4 Simulation results of sand particles limit ability of brick arrays with inlet friction velocity ($u_*=0.3$ m/s). (a), velocity contour plot of brick arrays; (b), trajectories of sand particles in brick arrays.

kept sand particles always near the surface and rapidly weakened the forward momentum, which was obviously more beneficial for sand encroachment protection. As a comparison, some sand particles may jump over 20 cm when they collided with the slides of straw checkerboard barriers, and the sand transport distances by wind increased significantly.

The mean velocity increased significantly on widening the horizontal space between bricks (Fig. 5a). When the longitudinal space became 0.4 m, the mean velocity decreased to a constant value and then increased slightly with increasing horizontal space (Fig. 5a). This is probably because when the air flowed through the bricks placed with a suitable longitudinal space, a series of eddies emerged within the brick arrays and a large amount of airflow energy was consumed near the surface. The mean velocity increased with the longitudinal size increased, and it decreased when the horizontal size or vertical size increased (Fig. 5b). It is clear that increasing the vertical size is a very effective method to reduce the mean velocity when the vertical size is less than 0.25 m. Thus, optimizing the brick space and size may most efficiently decrease the mean velocity of the air flow. Furthermore, the mean velocity increased linearly with the increase in friction velocity (Fig. 5c).

The variation in the invasion distance is shown in Figure 6a. Note that the invasion distance first decreased and then increased rapidly as the longitudinal space increased. Compared with Figure 5a, both lines turned to the lowest point when the longitudinal space was 0.4 m. This can be explained by the fact that most of the airflow power was used to form eddies between the bricks, and minority power remained to push the sand particles forward in this case. Figure 6b shows a

more complicated change in the invasion distance with changes in the brick size. The invasion distance significantly increased and then decreased with increasing vertical size. This may be explained by the fact that more airflow entered the interspaces between the bricks at the beginning and accelerated the wind flow. As the vertical size increased, the form drag of the bricks was significantly enhanced, which slowed down the velocity of airflow near the surface. Moreover, the brick arrays were better at blocking sand particles when the friction velocity was low (Fig. 6c). It is evident that an appropriate adjustment of the spaces and sizes of the bricks can significantly decrease the invasion distance normally by 3–4 m, which was slightly longer than the invasion distance of straw checkerboard barriers (Huang et al., 2013; Bo et al., 2015; Xu et al., 2018; Wang et al., 2020).

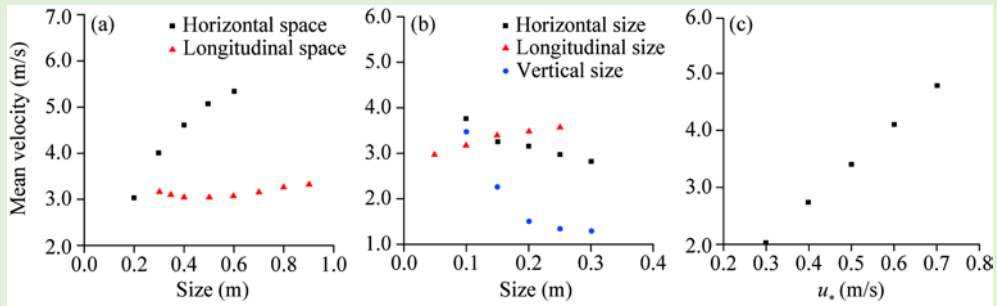


Fig. 5 Relationships of the mean air velocity versus (a) the space between bricks with $u_* = 0.3$ m/s, (b) the size of bricks with $u_* = 0.3$ m/s, and (c) the u_* , u_* , friction velocity.

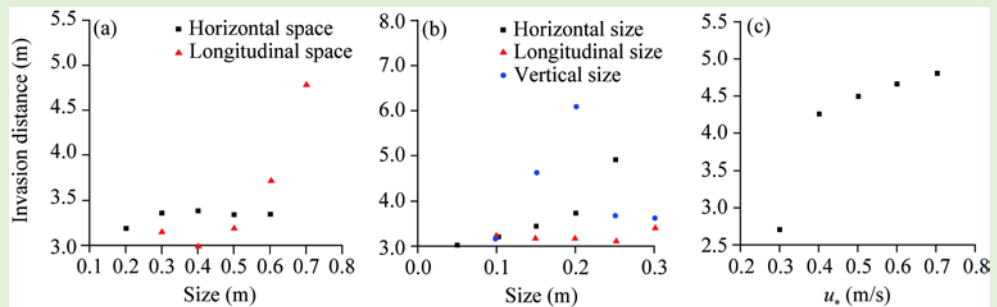


Fig. 6 Variations of the invasion distance versus (a) the space between bricks with $u_* = 0.3$ m/s, (b) the size of bricks with $u_* = 0.3$ m/s, and (c) the u_* .

3.2 Solar panel arrays

Another series of simulations were performed to evaluate the sand fixing and blocking performance of the solar panel arrays. As shown in Figure 7a, a series of eddies emerged within the solar panel arrays, and the velocity of airflow was significantly reduced in the same regions as the brick arrays. Figure 7b presents the movement characteristics of the sand particles around the solar panel arrays. Most of the sand particles rapidly passed through the interspaces between solar panel arrays, suggesting that the solar panel arrays are not so good for blocking sand as brick arrays. In contrast to the brick arrays, some sand particles can move above the solar panels owing to the solar panel laying an angle, and a few particles will deposit on them. This is a typical phenomenon in the application of solar panels, which exerted a negative effect on energy generation (Farid, 2012). Compared with the majority of previous studies focused on the pollutant effect of particles (Mani and Pillai, 2010; Kazem et al., 2014; Darwish et al., 2015), our simulation results reproduced the deposition process of sand particles on solar panels, which will be helpful for improving their energy utilization efficiency.

Figure 8 illustrates that changing the horizontal space, longitudinal space, or solar panel sizes had little effect on reducing the mean velocity unless the horizontal space was very small. In other

words, the solar panel arrays exhibited the best effect to fix and block the sand particles when the solar panels were close to a row of walls. Figure 8c shows that the mean velocity decreased when increasing the angle between the solar panels and the ground, and Figure 8d demonstrates that the mean velocity increased linearly with the increase in friction velocity. In general, the mean velocity increased in most cases because the solar panel arrays can increase the airflow entering the interspaces between the solar panels unless the horizontal space was very small, and can remove sand particles by enhancing the airflow in a specific configuration. Thus, the solar panel arrays played a flexible role in either blocking the incoming sand particles or removing the accumulation of sand particles in accordance with specific conditions.

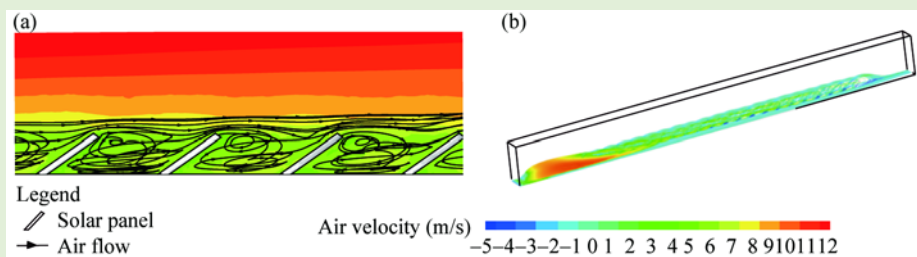


Fig. 7 Simulation results of sand particles limit ability of solar panel arrays with inlet friction velocity $u_* = 0.3$ m/s. (a), velocity contour plot of solar panel arrays; (b), trajectories of sand particles in solar panel arrays.

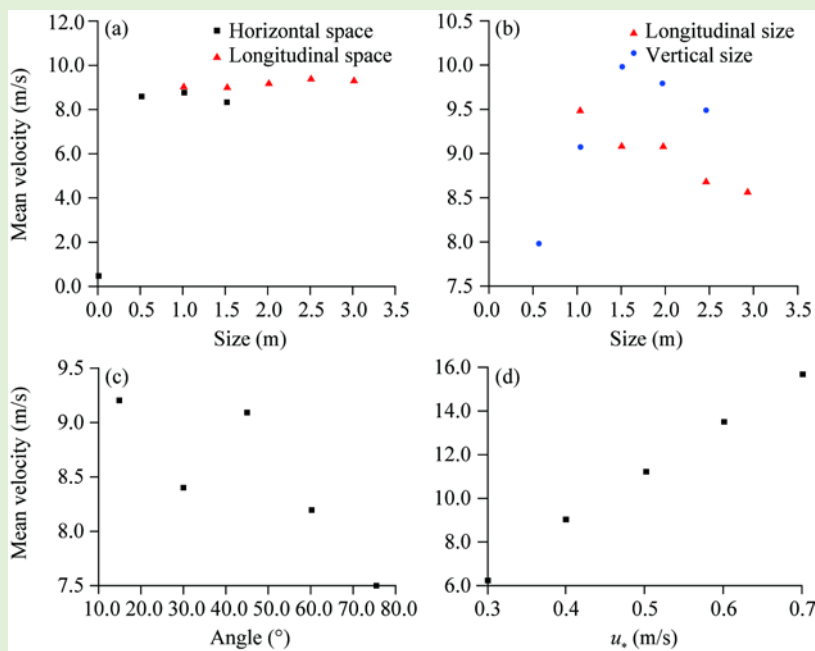


Fig. 8 Variations of the mean velocity versus (a) the space between panels with $u_* = 0.3$ m/s, (b) the sizes of panels with $u_* = 0.3$ m/s, (c) the angle between the panels and the ground with $u_* = 0.3$ m/s, and (d) the u_* .

3.3 Building arrays

Figure 9 presents the flow velocity field and the movement of sand particles in the building arrays. As shown in Figure 9a, a series of eddies emerged within the building arrays, and the velocity of airflow was significantly reduced in the same regions as the brick and solar panel arrays. The longitudinal space was replete with a large eddy when the longitudinal space was approximately equal to the brick height. This has also been observed by Kanda et al. (2004) in their laboratory Large-eddy simulation results, which confirmed the existence of isolated large eddy in canyon flow regimes. The building spacing was significantly larger than that of bricks in the described situation,

and the eddies had no chance to reduce the power of airflow near the surface between the arrays. Figure 9b shows that most sand particles rapidly passed through the interspaces between building arrays and only a few particles deposited in front of the buildings. This coincides with the transport and deposit characteristics of particulate pollutants in urban street canyons summarized by Yazid et al. (2014). Our results suggest that blown sand hazards had little effect on building arrays on a flat surface.

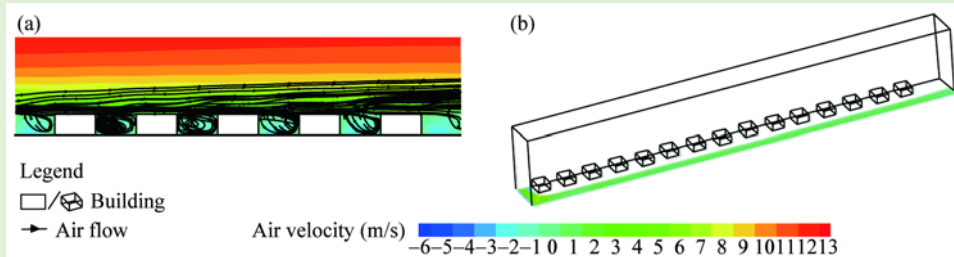


Fig. 9 Simulation results of sand particles limit ability of building arrays with inlet friction velocity $u_* = 0.3$ m/s. (a), velocity contour plot of building arrays; (b), trajectories of sand particles in building arrays.

Figure 10 illustrates that changing the horizontal space, longitudinal space, or building sizes had little effect on reducing the mean velocity in most cases. Similar to the situation with solar panel arrays, Figure 10a shows that the mean velocity was significantly reduced when the horizontal space was small, but it was still too high to prevent sand particles from moving. According to Figure 10b, the canyon effect was enhanced because of the increased vertical size and air flow entering the interspaces between the buildings. Therefore, the mean velocity evidently increased with the vertical size. Figure 10c shows that the mean velocity linearly increased with the friction velocity. Thus, there was no risk of buried damage from the sand flow when the building arrays were arranged in an appropriate configuration.

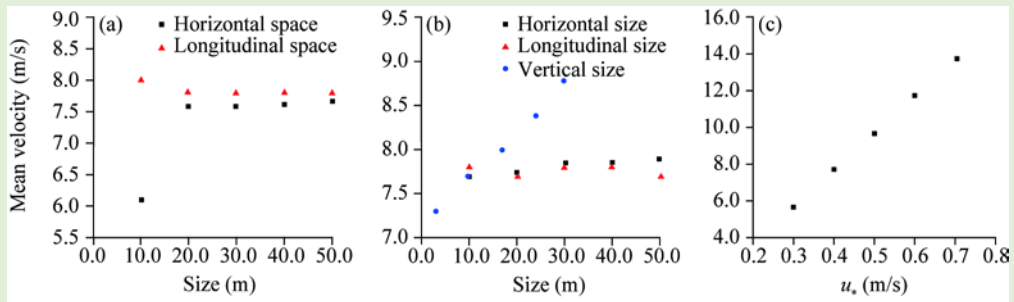


Fig. 10 Variations of the mean velocity versus (a) the space between buildings with $u_* = 0.3$ m/s, (b) the sizes of building with $u_* = 0.3$ m/s, and (c) the u_* .

3.4 Distribution of sand flux

Variations in the distribution of sand fluxes in the streamwise direction in brick arrays are shown in Figure 11 to investigate the influence of arrays on the development of wind-sand flow. Note that changes in the horizontal brick space and horizontal size between bricks had a significant influence on the sand-flux rate on the inlet owing to the complex boundary and flow field (Dun et al., 2018), and the influence decreased with the sand flow into the brick arrays. This is because the entering space for sand into brick arrays became smaller when we increased the horizontal size and decreased the horizontal space, and more sand particles resisted outside. However, the wind flow in the streamwise direction was hardly affected in these situations, and the sand fluxes and invasion distances were almost the same inside the brick arrays. Figure 11a shows that, although increasing the longitudinal space had a slight impact on the sand-flux rate on the inlet of the brick arrays, it increased the wind-flow structure in the streamwise direction inside the brick arrays, thereby

enhancing the sand-flux rates and invasion distances by providing more energy to the sand particles. Figure 11b illustrates that the sand flux reached its peak when the vertical size was approximately 0.2 m, indicating that this vertical size may strengthen the wind-flow structure and 0.1 m was a more proper vertical size for tiled barriers for sand encroachment protection (Bo et al., 2015; Xu et al., 2018). Figure 11c suggests that the brick arrays performed better when the sand-flux rate was reduced at a low friction velocity. Owing to the little effect on blocking sand particles in most situations, the distributions of sand flux in solar panels and building arrays were not the primary focus of this study.

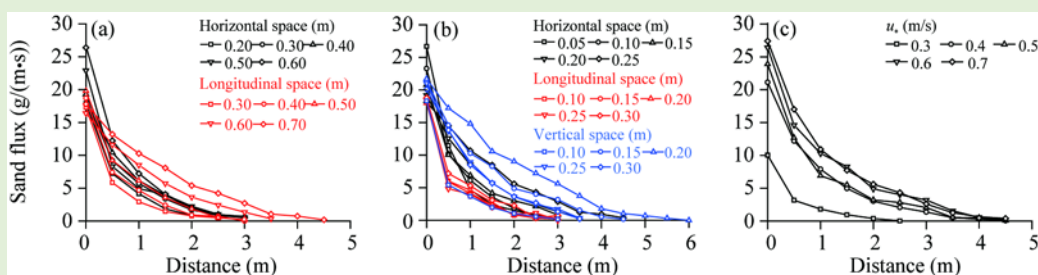


Fig. 11 Distribution of sand flux in streamwise direction in brick arrays versus (a) the space between bricks with $u_* = 0.3$ m/s, (b) the size of bricks with $u_* = 0.3$ m/s, and (c) the u_* .

3.5 Configuration considerations

In general, most of the settlements are composed of block, solar panel, and building arrays to meet the basic needs of humans. There are few other human facilities affecting wind flow and sand movement. In this case, the three types of arrays considered in this study should be the main focus of configuration consideration for human settlement.

The above results suggest that the brick arrays have the most significant effect on reducing the mean velocity of airflow and the invasion distance of sand particles, demonstrating good sand fixing and blocking performance. Both the solar panel and building arrays, however, can increase the mean velocity in most cases and block the deposition of most sand particles. Exceptionally, the solar panel arrays have a significant effect on fixing and blocking sand particles when the horizontal space is small. Consequently, brick arrays must be arranged in an upwind area to stop sand-particle movement and fix them on the ground. Solar panel arrays are supposed to accelerate the wind flow where sand particles deposit easily, and building arrays should better to be arranged in downwind areas.

4 Conclusions

The invasion distance and mean velocity significantly decreased in the space between the brick arrays with properly selected vertical size and interspace, indicating that the brick arrays have a remarkable sand fixing and blocking performance, and their effective protection distance is 3–4 m.

Concerning the simulation results of the solar panel arrays, the mean velocity increased in most cases unless the horizontal space was very small, and the sand particles could be removed by enhancing the airflow in a specific configuration. The deposition of sand particles on solar panels was simulated. This is beneficial to improve the energy utilization efficiency in future studies.

The large spaces of buildings hindered reducing the power of airflow near the surface between the arrays, resulting in most sand particles rapidly going through the interspaces between the building arrays and only a few particles deposited in front of the buildings. These results suggest that blown sand hazards have little effect on building arrays on a flat surface.

Hence, in consideration of the optimal configuration of settlement systems, this study concludes that: (1) brick arrays must be arranged in an upwind area; (2) solar panel arrays could accelerate the wind flow, so it is best to arrange them at the place where sand particles deposit easily; and (3) building arrays must be arranged in downwind areas.

Acknowledgements

This research was supported by the National Natural Science Foundation of China (11772143, 11702163, 41730644) and the National Key Research and Development Program of China (2016YFC0500901).

References

- Batchelor G K. 2000. *An Introduction to Fluid Dynamics*. Cambridge: Cambridge University Press, 241.
- Behrouzi F, Sidik N A C, Malik A M A, et al. 2014. Prediction of wind flow around high-rise buildings using RANS models. *Applied Mechanics and Materials*, 554: 724–729.
- Bitog J P, Lee I B, Shin M H, et al. 2009. Numerical simulation of an array of fences in Saemangeum reclaimed land. *Atmospheric Environment*, 43(30): 4612–4621.
- Blocken B. 2014. 50 years of computational wind engineering: past, present and future. *Journal of Wind Engineering and Industrial Aerodynamics*, 129: 69–102.
- Bo T L, Ma P, Zheng X J. 2015. Numerical study on the effect of semi-buried straw checkerboard sand barriers belt on the wind speed. *Aeolian Research*, 16: 101–107.
- Chen G H, Wang W W, Sun C F, et al. 2012. 3D numerical simulation of wind flow behind a new porous fence. *Powder Technology*, 230: 118–126.
- Chiu P H, Raghavan V S G, Poh H J, et al. 2017. CFD methodology development for Singapore green mark building application. *Procedia Engineering*, 180: 1596–1602.
- Christo F C. 2012. Numerical modelling of wind and dust patterns around a full-scale paraboloidal solar dish. *Renewable Energy*, 39(1): 356–366.
- Christopherson R W, Byrne M L, Aitken A E. 2002. *Geosystems: An Introduction to Physical Geography*. Upper Saddle River: Prentice Hall, 52.
- Darwish Z A, Kazem H A, Sopian K, et al. 2015. Effect of dust pollutant type on photovoltaic performance. *Renewable and Sustainable Energy Reviews*, 41: 735–744.
- Dun H C, Huang N, Zhang J, et al. 2018. Effects of shape and rotation of sand particles in saltation. *Journal of Geophysical Research: Atmospheres*, 123(23): 13,462–13,471.
- Golany G. 1978. *Urban Planning for Arid Zones: American Experiences and Directions*. New York: John Wiley & Sons, Inc., 142–146.
- Hatanaka K, Hotta S. 1997. Finite element analysis of air flow around permeable sand fences. *International Journal for Numerical Methods in Fluids*, 24: 1291–1306.
- Huang N, Zheng X J, Zhou Y H, et al. 2006. Simulation of wind-blown sand movement and probability density function of lift-off velocities of sand particles. *Journal of Geophysical Research: Atmospheres*, 111: D20201, doi: 10.1029/2005JD006559.
- Huang N, Xia X P, Tong D. 2013. Numerical simulation of wind sand movement in straw checkerboard barriers. *The European Physical Journal E*, 36: 99, doi: 10.1140/epje/i2013-13099-6.
- Huang N, Gong K, Xu B, et al. 2019. Investigations into the law of sand particle accumulation over railway subgrade with wind-break wall. *The European Physical Journal E*, 42: 145, doi: 10.1140/epje/i2019-11910-0.
- Hunter L J, Watson I D, Johnson G T. 1990. Modeling air flow regimes in urban canyons. *Energy Build*, 15: 315–324.
- Jiang H, Dun H C, Tong D, et al. 2017. Sand transportation and reverse patterns over leeward face of sand dune. *Geomorphology*, 283: 41–47.
- Kanda M, Moriawaki R, Kasamatsu F. 2004. Large-eddy simulation of turbulent organized structures within and above explicitly resolved cube arrays. *Boundary-Layer Meteorology*, 112: 343–368.
- Kazem A A, Chaichan M T, Kazem H A. 2014. Effect of dust on photovoltaic utilization in Iraq: review article. *Renewable and Sustainable Energy Reviews*, 37: 734–749.
- Lee S J, Lim H C. 2001. A numerical study on flow around a triangular prism located behind a porous fence. *Fluid Dynamics Research*, 28: 209–221.
- Lien F S, Yee E, Cheng Y. 2004. Simulation of mean flow and turbulence over a 2D building array using high-resolution CFD and a distributed drag force approach. *Journal of Wind Engineering and Industrial Aerodynamics*, 92(2): 117–158.
- Liu H J, Wang J H, Li Y, et al. 2011. Effects of plastic checkerboard sand-barrier on wind-sand flux of leeward of crescentic dune. *Journal of Soil and Water Conservation*, 25(5): 26–29, 34. (in Chinese)
- Mani M, Pillai R. 2010. Impact of dust on solar photovoltaic (PV) performance: research status, challenges and recommendations. *Renewable and Sustainable Energy Reviews*, 14: 3124–3131.
- Mohamed A M I, Khalaf F I. 2005. Development of computer software for the calculation of the rate of aeolian sand transport.

- Port-Said Engineering Research Journal, 9: 251–266.
- Montazeri H, Blocken B. 2013. CFD simulation of wind-induced pressure coefficients on buildings with and without balconies: validation and sensitivity analysis. *Building and Environment*, 60: 137–149.
- Pye K, Tsoar H. 2009. *Aeolian Sand and Sand Dunes*. Berlin: Springer Berlin Heidelberg, 329–367, <https://link.springer.com/book/10.1007%2F978-3-540-85910-9>.
- Ramponi R, Blocken B. 2012. CFD simulation of cross-ventilation for a generic isolated building: impact of computational parameters. *Building and Environment*, 53: 34–48.
- Raupach M R, Thom A S, Edwards I. 1980. A wind-tunnel study of turbulent flow close to regularly arrayed rough surfaces. *Boundary-Layer Meteorology*, 18: 373–397.
- Raupach M R, Lu H. 2004. Representation of land-surface processes in aeolian transport models. *Environmental Modelling & Software*, 19(2): 93–112.
- Sun T, Liu H J, Zhu G Q, et al. 2012. Timeliness of reducing wind and stabilizing sand functions of three mechanical sand barriers in arid region. *Journal of Soil and Water Conservation*, 26(4): 12–16, 22. (in Chinese)
- Tian L H, Wu W Y, Zhang D S, et al. 2015. Characteristics of erosion and deposition of straw checkerboard barriers in alpine sandy land. *Environmental Earth Sciences*, 74: 573–584.
- Tsuchiya K, Igarashi T, Qong M. 2010. Land cover change detection based on satellite data for an arid area to the south of Aksu in Taklimakan desert. *Journal of Arid Land*, 2(1): 14–19.
- Wang T, Qu J J, Ling Y Q, et al. 2017. Wind tunnel test on the effect of metal net fences on sand flux in a Gobi Desert, China. *Journal of Arid Land*, 9(6): 888–899.
- Wang T, Qu J J, Niu Q H. 2020. Comparative study of the shelter efficacy of straw checkerboard barriers and rocky checkerboard barriers in a wind tunnel. *Aeolian Research*, 43: 100575, doi: 10.1016/j.aeolia.2020.100575.
- Wang Z T, Zheng X J. 2002. A simple model for calculating measurements of straw checkerboard barriers. *Journal of Desert Research*, 22(3), 229–232. (in Chinese)
- Warner T T. 2004. *Desert Meteorology*. Cambridge: Cambridge University Press, 1–4.
- Xu B, Zhang J, Huang N, et al. 2018. Characteristics of turbulent aeolian sand movement over straw checkerboard barriers and formation mechanisms of their internal erosion form. *Journal of Geophysical Research: Atmospheres*, 123: 6907–6919.
- Yakhot V, Orszag S A. 1986. Renormalization group analysis of turbulence. I. basic theory. *Journal of Scientific Computing*, 1(1): 3–49.
- Yazid A W M, Sidik N A C, Salim S M, et al. 2014. A review on the flow structure and pollutant dispersion in urban street canyons for urban planning strategies. *Simulation*, 90(8): 892–916.
- Zhang N, Kang J H, Lee S J. 2010. Wind tunnel observation on the effect of a porous wind fence on shelter of saltating sand particles. *Geomorphology*, 120(3–4): 224–232.
- Zhao W J, Wang L R, Ji H, et al. 2012. Effect of blended wheat straw on evaporation of seeding bricks with different soils. *Bulletin of Soil and Water Conservation*, 32(5): 253–256. (in Chinese)